Research article

Jinwen Song, Shuai Yuan, Chengcong Cui, Yuxi Wang, Zhiyong Li, Alan X. Wang, Cheng Zeng* and Jinsong Xia*

High-efficiency and high-speed germanium photodetector enabled by multiresonant photonic crystal

Abstract: High-efficiency and high-speed photodetectors with broadband responses are playing pivotal roles for wavelength-division multiplexing optical communications. Germanium photodetectors on silicon platforms exhibit potential cost advantage due to the compatibility for monolithic integration with silicon-based electronic circuits for signal amplification and processing. In this article, we report a normal incidence, germanium photodetector enabled by guided-mode resonances in photonic crystal, which successfully resolved the compromise between quantum efficiency, wavelength coverage and bandwidth requirement, a drawback usually faced by conventional photodetectors operating at normal incidence. The resonant photonic crystal structure is designed to support multiple resonances in the target wavelength range. With an intrinsic absorption layer thickness of 350 nm, the device achieved a high external quantum efficiency of 50% at 1550 nm, along with an enhancement around 300% for the entire C-band. Using a mesa diameter of 14 μm, the fabricated device exhibited a 3-dB bandwidth of 33 GHz and obtained clear eye diagrams at bit rate up to 56 Gbps. This work provides a

promising method to design high-efficiency, high-speed, normal incidence germanium photodetectors for optical interconnect systems.

1 Introduction

Silicon photonics is a very promising platform which can not only produce compact, low power, multifunctional photonic circuits but also allow such photonic circuits to be built on the same chip as the microelectronics [1–3]. Although the indirect band gap of group IV elements blocks their applications in semiconductor lasers [4, 5], silicon-germanium (Si–Ge) photodetectors [6–10] have been playing increasing roles in optical communications. Particularly, the cost efficiency of normal incidence photodetectors is urging their extensive research and applications.

Currently, normal incidence photodetectors used in the telecommunication window are dominated by III–V compound semiconductors [11] due to their small dark current and high quantum efficiency, despite the fact that this platform is not CMOS compatible. In comparison, CMOS-compatible Ge photodetectors are limited by the low absorption efficiency at C-band. A general approach to enhance the responsivity is increasing the thickness of the intrinsic absorption layer. However, a thick intrinsic layer will result in a long transit time of photon-generated carriers, limiting the bandwidth of Ge photodetectors. To overcome the trade-off between quantum efficiency and bandwidth in normal incidence Ge photodetectors, different methods have been adopted to enhance the photon responsivity. The Fabry–Perot cavity is a traditional way to enhance the light–matter interactions by trapping light inside. A number of resonant-cavity-enhanced (RCE) photodetectors have been demonstrated [12–15], employing

Jinwen Song and Shuai Yuan are contributed equally to this work.

*Corresponding authors: Cheng Zeng and Jinsong Xia, Wuhan National Laboratory for Optoelectronics, Huazhong University of Science and Technology, Wuhan, 430074, China,
E-mail: zengchengwuli@hust.edu.cn (C. Zeng), jsxia@hust.edu.cn (J. Xia). https://orcid.org/0000-0002-9650-7839
Jinwen Song, Shuai Yuan, Chengcong Cui and Yuxi Wang, Wuhan National Laboratory for Optoelectronics, Huazhong University of Science and Technology, Wuhan, 430074, China
Zhiyong Li, State Key Laboratory of Integrated Optoelectronics, Institute of Semiconductors, Chinese Academy of Sciences, Beijing, 100083, China
Alan X. Wang, School of Electrical Engineering and Computer Science, Oregon State University, Corvallis, OR, 97331, USA

Fabry–Perot cavity formed by distributed Bragg reflectors or metal reflectors. Although effective in responsivity enhancement, RCE photodetectors are intrinsically wavelength sensitive. In addition, two previous works have simulated enhanced light absorption enabled by guided-mode resonance (GMR) in Ge photodetectors [16, 17]. In these works, photonic crystal (PhC) is introduced to bring with single GMR at the target wavelength range, leading to a narrow-band light absorption enhancement. One method to achieve a wide spectrum responsivity is to incorporate tin (Sn) into Ge crystals, forming GeSn alloy. The bandgap of GeSn crystal shifts to longer wavelengths than Ge [18–20], resulting in larger absorption efficiency at C-band. However, the dark current of GeSn photodetectors increases with Sn content due to the reduction of the GeSn bandgap [21] and the increase of defect density [19].

Therefore, there is a desire to implement normal-incident Ge photodetectors to achieve high speed and high efficiency across the whole C-band. In this article, we present a normal incidence Ge-on-Si PIN photodetector with a 350 nm intrinsic layer, which employs GMRs to enhance the light absorption. A high responsivity of 0.62 A/W is achieved at 1550 nm. In addition, a PhC structure is designed to excite overlapped multiple resonances to broaden the wavelength coverage, leading to EQE around 50% across the whole C-band. With a mesa diameter of 14 μm, the fabricated device exhibits a 3-dB bandwidth of 33 GHz and obtains clear eye diagrams at bit rate up to 56 Gbps. These characteristics compare favorably with previous reports, as shown in Supplementary Section V.

2 Device design and analysis

Optical resonance is widely used to enhance light–matter interactions [22–26] as it increases local field intensity. The combination of resonant structures and photodetectors can strongly enhance the optical responsivity [17, 27, 28]. However, one key characteristic of resonance is wavelength selectivity. Multiple resonances can be employed to broaden the wavelength coverage, which requires that the resonant structure can support multiple resonances overlapping each other.

The GMRs in PhC have been widely employed in applications including photodetectors [29–32], low threshold lasers [33] and optical filters [34, 35]. Specially, multi-GMRs in PhC have been used to realize wide-band filters. GMR can provide not only an efficient way to channel light from free space to within the PhC slab, but also strong enhancement of the local field [36]. As a result, realizing a normal incident photodetector from a PhC with

multiple resonances will lead to enhanced absorption in a wide wavelength range. Another important characteristic of GMR is that strong optical resonances can be achieved in PhC with only a few periods [37], which enables the use of GMRs in small-size photodetectors for high-speed applications.

The proposed Ge photodetector with resonant PhC is a mesa-type PIN photodetector based on silicon-on-insulator (SOI) platform. Details of the structure are schematically shown in Figure 1(a). The thicknesses of the top Si and buried oxide (BOX) layers of the SOI wafer are 200 nm and 2 μm, respectively. A 100 nm p$^+$–Si buffer layer is grown by molecular beam epitaxy (MBE), followed by a 100 nm p$^+$–Ge layer, a 350 nm i–Ge layer, a 50 nm n$^+$–Ge layer and a 25 nm n$^+$–Si layer. The absorption region is the i–Ge layer and has a thickness of only 350 nm to minimize the transit time of carriers. The designed resonant PhC is a two-dimensional periodic structure located at the center of the photodetector. Subwavelength scale holes are etched into the mesa surface to a depth of around 215 nm. The holes are uniform cylinders and formed in square lattices. A 300 nm SiO$_2$ layer is deposited by plasma-enhanced chemical vapor deposition (PECVD) on top to passivate and protect the devices. The larger refractive index contrast between Si/Ge and SiO$_2$ provides the necessary field confinement for optical resonances in the PhC. In this work, the photodetectors are fabricated with mesa diameters of 30 and 14 μm. Devices on the same wafer as reference PDs without PhC structure are also fabricated. Figure 1(b–e) shows the SEM images for the patterned PDs. Detailed fabrication processes are available in Supplementary Section IV.

To understand the role of GMRs in our structure, a simulation is conducted on an infinite two-dimensional PhC using the finite-difference time-domain (FDTD) method with periodic boundary condition. The holes are arranged in the x-y plane, as shown in Figure 2(a). For polarization independence, the hole-array is given the same period in the x and y directions. The period, etching depth and diameter of the holes are optimized to achieve multiple resonant modes spreading across the C-band. The permittivity of Ge used in FDTD simulations is experimentally measured using spectroscopic ellipsometer. When the illumination is a y-polarized plane wave at normal incident, multiple GMRs at the Γ point are excited. Calculated absorption spectra of the resonant PhC and the reference structure with no PhC are shown in Figure 2(b). A strong absorption enhancement is obvious in the wavelength range from 1480 to 1580 nm, with four resonance peaks at 1485, 1521, 1550 and 1574 nm, which are marked as mode I, II, III and IV. The dispersion relation of these four
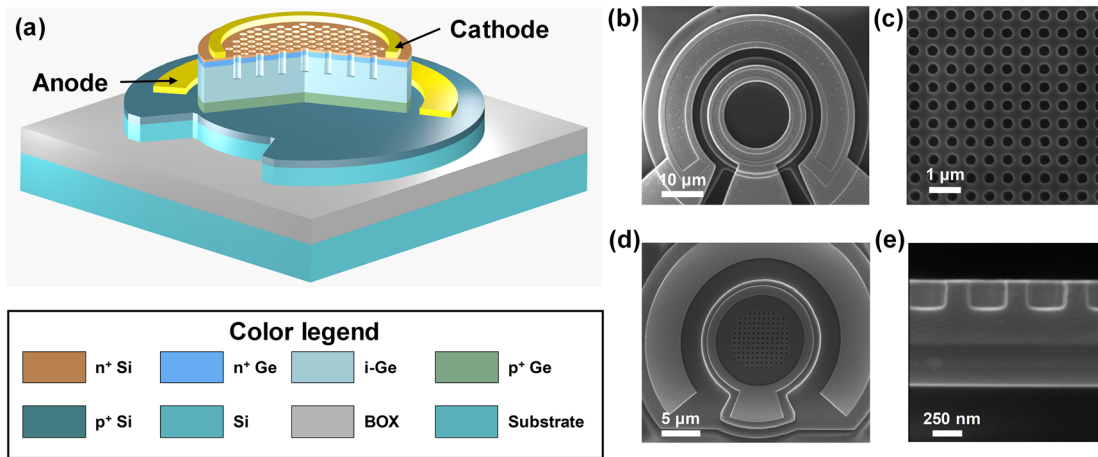
Figure 1: Germanium photodetector enabled by resonant-PhC.
(a) Schematic of the resonant-PhC germanium photodetector with an ultrathin absorbing layer (absence of the top SiO$_2$ layer for clear depiction). Materials of different layers from top to bottom: n$^+$–Si layer, n$^+$–Ge layer, i–Ge layer, p$^+$–Ge layer, p$^+$–Si layer, top Si layer of SOI, BOX of SOI, Si substrate of SOI. (b) Scanning-electron-microscope (SEM) image of a 30-μm-diameter Ge PD with PhC. (c) Enlarged image of the resonant PhC integrated in the photodetectors. (d) SEM image of a 14-μm-diameter Ge PD with PhC. (e) Cross section of the resonant PhC etched into the i–Ge layer of the photodetector.

GMRs around Γ point is given in Supplementary Section I. Wide spectral width of these resonances primarily comes from the material absorption of Ge. Figure 2(c) shows the electric/magnetic field intensity distributions of these resonant modes. It is seen that most of the electric/ magnetic field is confined in the high index layers of Ge and Si. Consequently, the resonance-mode-trapped photons are gradually absorbed in the Ge layer. More discussion of these four resonant modes is given in Supplementary Sections II and III.
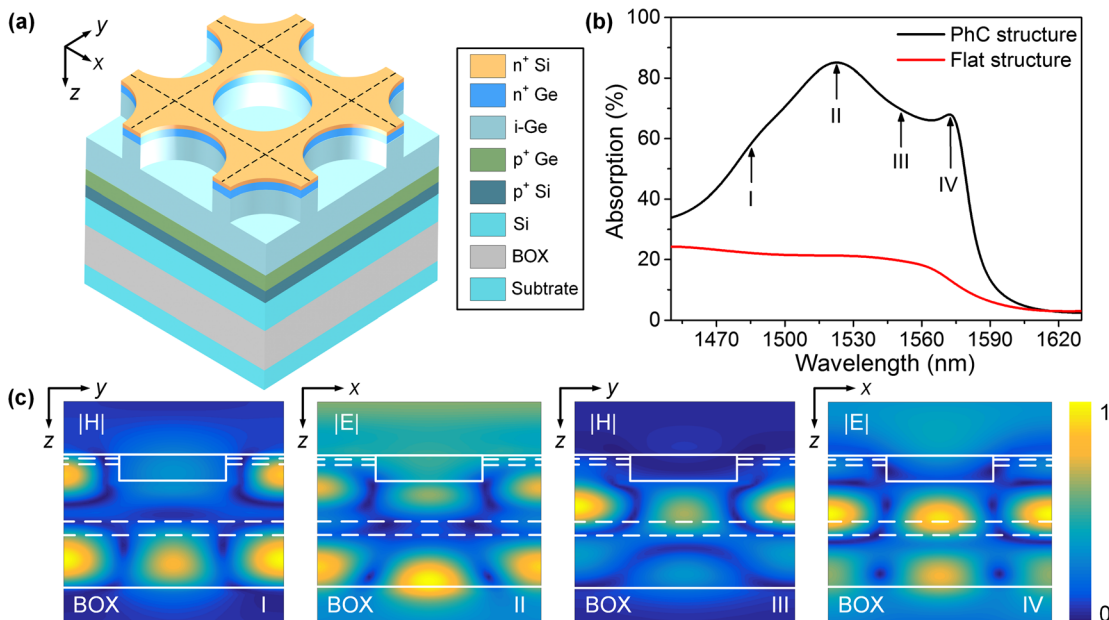

Figure 2: FDTD simulation of resonant PhC.
(a) One unit cell of the periodic hole (the square denoted by the dashed line). (b) Calculated absorption spectra of the PhC and flat structure. Period, hole diameter and etching depth are 540, 300 and 215 nm, respectively. (c) The normalized electric (mode II and IV) and magnetic (mode I and III) field intensity distributions of the four GMRs along cross sections in the *x-z* and *y-z* planes. Dashed lines indicate the doped Ge regions.

3 Demonstration of enhanced external quantum efficiency

3D-FDTD simulation is performed on the Ge photodetector. Diameter of the device mesa is 30 μm, which is the same as the experimentally fabricated device. Period, diameter and etching depth of the hole-array are extracted from the SEM images. Simulated absorption spectra of the device are shown in Figure 3(a), which show greatly enhanced absorption efficiencies compared with the reference PD. The results are not as good as the calculated results of the infinite structure in Figure 2(b), as the illumination is now a Gaussian beam with a spot diameter of 10 μm and the size of the PhC is limited by the device mesa. As the size of the incident spot is smaller than that of the PhC, effective region of the PhC is the area covered by the incident spot. Light leakage at the edges of the effective region weakens the strength of optical resonances [38, 39]. Visualized comparisons between the optical responses in the patterned PD and the reference PD are provided in the Supplementary Section VIII.

Experimentally measured EQEs of a 30-μm-diameter patterned PD and the reference PD are shown in Figure 3(a). Light from a tunable laser is coupled to the

PDs using a standard single-mode fiber (SMF-28e, spot diameter = 10 μm). The EQEs are greatly enhanced in the wavelength range from 1500 to 1550 nm (EQE > 50%). A peak EQE value of 62% is achieved at 1530 nm. Measured EQEs of the patterned PD are lower than the simulated results. Main reason for this discrepancy is the doped Ge layers, where the photogenerated carriers can hardly contribute to the photocurrents, due to the weak electric field in the doped regions. Thickness of the intrinsic layer is 350 nm out of the total 500 nm Ge, which means a considerable part of the incident photon will be dissipated in the doped regions. Detailed calculation is given in the Supplementary Section VII.

Figure 3(b) and (c) shows the EQEs and the corresponding enhancement of the fabricated PDs with different hole-array periods, respectively. Strongly enhanced EQE is realized in a wide wavelength range. The peak wavelength red-shifts as the PhC period increases with peak EQE enhancement around 350%. Comparing the EQE enhancement results between the devices with period of 520 and 540 nm, we can find that mode IV of the 520-nm-period device coincides with mode II of the 540-nm-period device. However, the EQE enhancement of mode II is higher than that of mode IV. Ignoring the slight difference in PhC period,
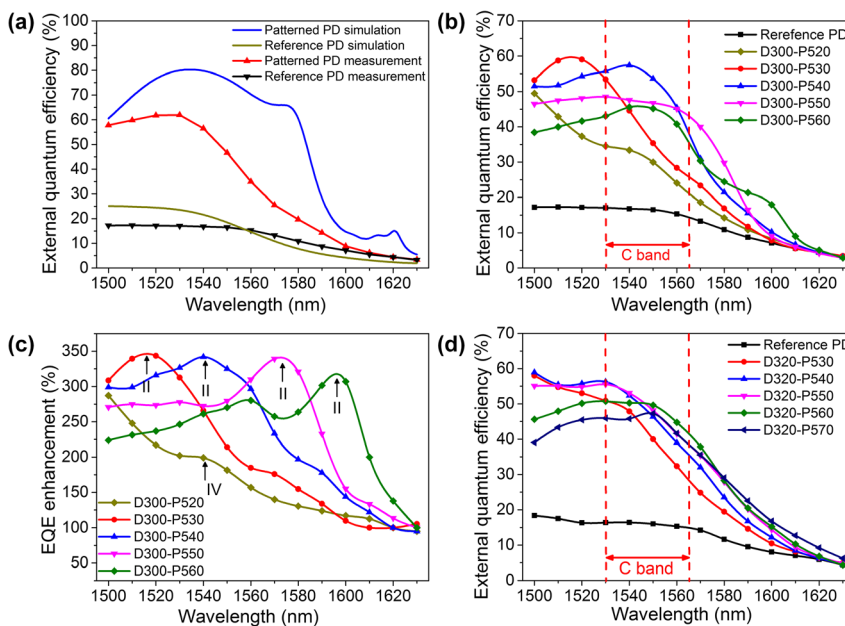

Figure 3: Enhanced external quantum efficiency of the patterned PD.
(a) FDTD simulated and experimentally measured EQE spectra of the 30-μm-diameter patterned PD. Diameter/period of the hole-array is 320/540 nm. Measured EQE is 57% at 1540 nm, while the simulated one is as high as 80% around 1540 nm. Both results show strongly enhanced absorption compared with the reference PD, respectively. (b–c) Measured EQE spectra (b) and the corresponding EQE enhancement spectra (c) for the 30-μm-diameter patterned PDs as the hole-array (hole diameter: 300 nm) period increases from 520 to 560 nm, exhibiting peak enhancement of more than 300% from 1500 to 1600 nm. The wavelength of the EQE peak increases approximately linearly with the period. (d) Measured responsivity spectra for the 14-μm-diameter patterned PDs as the hole-array (hole diameter: 320 nm) period increases from 530 to 570 nm.

the reason of this discrepancy in enhancement can only come from the different field distributions of mode II and mode IV. As shown in Figure 2(c), the overlap between the field and the doped regions for mode IV is much larger than that for mode II.

Figure 3(d) shows the measured optical responses of the 14-μm-diameter patterned PDs, where the diameter of the circular PhC region is around 7 μm. A tapered lensed fiber is used to focus the incident light spot diameter to 6 μm. As we can see, the optical responses exhibit similar results as the 30-μm-diameter patterned PDs. While the resonance peaks are not that clear as compared with that in Figure 3(b). When the size of effective region decreases, the strength of collective resonance in the PhC decreases as the proportion of light leakage from edges becomes larger and the resonance effect gets weaker [38, 39]. Moreover, the smaller incident spot size from the tapered lensed fiber has a worse uniformity than that of the standard single-mode fiber, which also degrades the performance of the multiresonances. Despite the existence of these nonideal effects, around 3 times enhancement of EQE is universally achieved in the wavelength range from 1500 to 1565 nm, covering the whole C-band. Specially, the highest EQE at 1550 nm is 50%. At the same time, the fact that the mesa is small means that the junction capacitance is small, which is critical for high-speed photodetectors.

4 The I–V characteristics and high-speed performance

Figure 4(a) shows the I–V characteristics of the 14-μm-diameter patterned PD and reference PD. The patterned PD exhibits a dark current of 58 nA at –1 V, corresponding to dark current density of 32 mA/cm^2. In comparison, the dark current and dark current density of the reference PD are 52 nA and 29 mA/cm^2, respectively. The results for the patterned PD and reference PD are approximate, implying that the shallow-etched holes of the patterned PD result in only a modest increase in the dark current.

Normalized frequency responses of the 14-μm-diameter patterned PD are measured by a vector network analyzer (Anritsu MS4647B). Modulated light at 1550 nm is coupled to the device using standard single-mode fiber, while the electrical output is measured through a high-speed RF probe. As shown in Figure 4(b), the 3-dB bandwidths of the device are 18, 33, and 33 GHz at bias of 0, –3 and –5 V, respectively. The high bandwidth is mainly attributed to the small junction capacitance. Changing the voltage from –3 to –5 V has negligible effect upon the 3 dB bandwidth of the PDs, which is consistent with the photogenerated carriers already reaching saturation velocity at –3 V.

Eye diagrams are measured at different bit rates to characterize the high-speed performance of the patterned PD. The laser at 1550 nm is modulated into a long optical nonreturn-to-zero pseudorandom bit sequence data pattern, using a commercial optical modulator. Output eye diagrams are recorded by a digital communication analyzer (DCA: Agilent 86100C). Transimpedance amplifier is not used in the measurements. As shown in Figure 4(c), eye diagrams at 25, 32, 40, 50 and 56 Gbps are obtained at a bias of –3 V. Q-factors of each eye diagram are measured at the same time. Specially, the bit error rate (BER) of the 56 Gbps eye diagram is 1.9×10^{-3} for the patterned PD, which is below the hard decision forward error coding (HD-FEC) limit (3.8×10^{-3}) [40]. These results reveal good high-speed performance of the patterned PD.
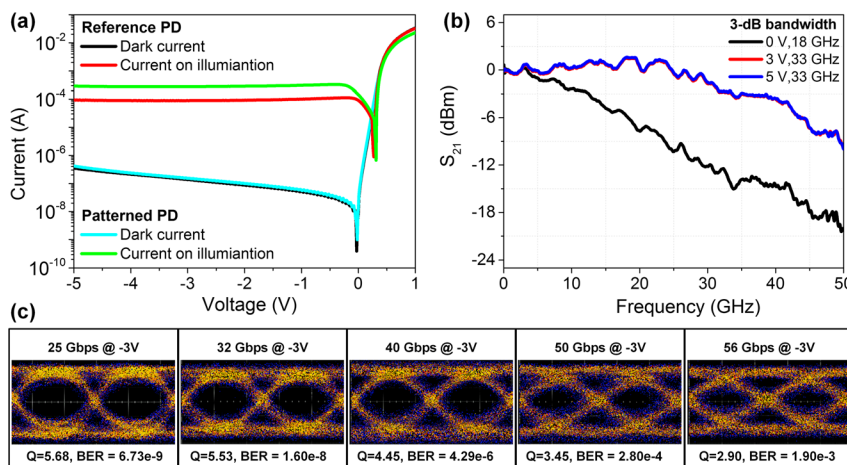

Figure 4: Electrical characterization of the 14-μm-diameter reference PD and patterned PD (period: 560 nm, diameter: 320 nm). (a) I–V characteristics of the patterned PD and the reference PD. Incident optical power is 0.5 mW at 1550 nm. (b) Normalized frequency responses of the patterned PD at 1550 nm. (c) Measured eye-diagrams of the patterned PD at 25, 32, 40, 50 and 56 Gbps (bias: –3 V). BER of each eye diagram is calculated from the Q-factor using the complementary error function.

5 Conclusion

We have demonstrated a high-efficiency, high-speed, normal incidence, Ge photodetector with PhC on a silicon platform. The EQE is enhanced by 300% by trapping the incident photons in the GMRs supported by the PhC. Wavelength coverage of the enhancement is broadened by multiple resonant modes spreading across the entire C-band. High external quantum efficiency around 50% for the whole C-band and a high responsivity of 0.62 A/W at 1550 nm are achieved for the 14-μm-diameter patterned PD with an ultrathin intrinsic Ge layer of 350 nm. In addition, the clear eye diagram exhibits a BER of 1.9×10^{-3} at the speed of 56 Gbps, confirming the high-speed performance of the device. Our work promotes the development of efficient, high-speed Ge photodetector compatible for monolithic integration with electronic integrated circuits, which has great potential to reduce the cost and power consumption for optical communications.

6 Methods

6.1 Epitaxial growth and device fabrication

Devices fabrication start with epitaxial growth on (100) SOI substrates, with 220 nm top Si and 2 μm buried oxide layer, in a solid molecular beam epitaxy chamber (Omicron EVO-50). Patterns of the devices are fabricated using electron beam lithography (Vistec EBPG 5000 Plus) and inductively coupled plasma (Oxford Plasmalab System 100 ICP180). Detailed epitaxial growth and device fabrication processes are showed in Supplementary Information.

6.2 EQE measurement

EQE measurements are conducted using Santec tunable semiconductor laser TSL-510 with 1 pm resolution. Two kinds of standard single-mode fibers are used to deliver the light to the PDs, with spot diameter of 10 and 6 μm. A precision source/measure unit (KEYSIGHT B2901A) is used to measure the I–V curve and photocurrent of the PDs.

6.3 Data availability

All relevant data are available from the corresponding author upon reasonable request.

References

[1] D. Thomson, A. Zilkie, J. E. Bowers, et al., "Roadmap on silicon photonics," *J. Opt.*, vol. 18, no. 7, p. 073003, 2016.

[2] B. Jalali and S. Fathpour, "Silicon photonics," *J. Lightwave Technol.*, vol. 24, no. 12, pp. 4600–4615, 2006.

[3] S. R. Forrest, "Monolithic optoelectronic integration: A new component technology for lightwave communications," *IEEE Trans. Electron. Dev.*, vol. 32, no. 12, pp. 2640–2655, 1985.

[4] E. M. Fadaly, A. Dijkstra, J. R. Suckert, et al., "Direct-bandgap emission from hexagonal Ge and SiGe alloys," *Nature*, vol. 580, no. 7802, pp. 205–209, 2020.

[5] R. Soref, D. Buca, and S.-Q. Yu, "Group IV photonics: driving integrated optoelectronics," *Opt. Photonics News*, vol. 27, no. 1, pp. 32–39, 2016.

[6] Y. Kang, H.-D. Liu, M. Morse, et al., "Monolithic germanium/silicon avalanche photodiodes with 340 GHz gain–bandwidth product," *Nat. Photonics*, vol. 3, no. 1, p. 59, 2009.

[7] J. Michel, J. Liu, and L. C. Kimerling, "High-performance Ge-on-Si photodetectors," *Nat. Photonics*, vol. 4, no. 8, p. 527, 2010.

[8] B. Shi, F. Qi, P. Cai, et al., "106 Gb/s normal-incidence Ge/Si avalanche photodiode with high sensitivity," in *Optical Fiber Communication Conference*, San Diego, California, USA, Institute of Electrical and Electronics Engineers, 2020.

[9] S. A. Srinivasan, J. Lambrecht, M. Berciano, et al., "Highly sensitive 56 Gbps NRZ O-band BiCMOS-silicon photonics receiver using a Ge/Si avalanche photodiode," in *Optical Fiber Communication Conference*, San Diego, California, USA, Institute of Electrical and Electronics Engineers, 2020.

[10] H. Chen, M. Galili, P. Verheyen, et al., "100-Gbps RZ data reception in 67-GHz Si-contacted germanium waveguide pin photodetectors," *J. Lightwave Technol.*, vol. 35, no. 4, pp. 722–726, 2016.

[11] T.-P. Lee, C. Burrus, and A. Dentai, "InGaAs/InP pin photodiodes for lightwave communications at the 0.95–1.65 μm wavelength," *IEEE J. Quant. Electron.*, vol. 17, no. 2, pp. 232–238, 1981.

[12] J. Chen and Z. Zhou, "Ultranarrow band and high-quantum-efficiency photoresponse of Ge-on-Si photodetectors using cascaded-cavity structure," *Appl. Phys. Lett.*, vol. 89, no. 4, p. 043126, 2006.

[13] O. I. Dosunmu, D. D. Cannon, M. K. Emsley, L. C. Kimerling, and M. S. Unlu, "High-speed resonant cavity enhanced Ge photodetectors on reflecting Si substrates for 1550-nm operation," *IEEE Photonics Technol. Lett.*, vol. 17, no. 1, pp. 175–177, 2005.

[14] M. Huang, S. Li, P. Cai, et al., "Germanium on silicon avalanche photodiode," *IEEE J. Sel. Top. Quant. Electron.*, vol. 24, no. 2, pp. 1–11, 2018.

[15] K. C. Balram, R. M. Audet, and D. A. B. Miller, "Nanoscale resonant-cavity-enhanced germanium photodetectors with lithographically defined spectral response for improved performance at telecommunications wavelengths," *Opt. Express*, vol. 21, no. 8, pp. 10228–10233, 2013.

[16] A. Y. Zhu, S. Zhu, and G.-Q. Lo, "Guided mode resonance enabled ultra-compact germanium photodetector for 1.55 μm detection," *Opt. Express*, vol. 22, no. 3, pp. 2247–2258, 2014.

[17] Z. Liu, J. Liu, B. Cheng, et al., "Enhanced light trapping in Ge-on-Si-on-insulator photodetector by guided mode resonance effect," *J. Appl. Phys.*, vol. 124, no. 5, p. 053101, 2018.

[18] M. Oehme, K. Kostecki, K. Ye, et al., "GeSn-on-Si normal incidence photodetectors with bandwidths more than 40 GHz," *Opt. Express*, vol. 22, no. 1, pp. 839–846, 2014.

[19] H. Tseng, H. Li, V. Mashanov, et al., "GeSn-based pin photodiodes with strained active layer on a Si wafer," *Appl. Phys. Lett.*, vol. 103, no. 23, p. 231907, 2013.

[20] J. Zheng, Z. Liu, C. Xue, et al., "Recent progress in GeSn growth and GeSn-based photonic devices," *J. Semiconduct.*, vol. 39, no. 6, p. 061006, 2018.

[21] Y. Dong, W. Wang, D. Lei, et al., "Suppression of dark current in germanium-tin on silicon p-i-n photodiode by a silicon surface passivation technique," *Opt. Express*, vol. 23, no. 14, pp. 18611–18619, 2015.

[22] Y.-Y. Lai, Y.-P. Lan, and T.-C. Lu, "Strong light–matter interaction in ZnO microcavities," *Light: Sci. Appl.*, vol. 2, p. e76, 2013.

[23] T. Tanabe, M. Notomi, E. Kuramochi, A. Shinya, and H. Taniyama, "Trapping and delaying photons for one nanosecond in an ultrasmall high-Q photonic-crystal nanocavity," *Nat. Photonics*, vol. 1, no. 1, pp. 49–52, 2007.

[24] N. P. de Leon, B. J. Shields, C. L. Yu, et al., "Tailoring light-matter interaction with a Nanoscale plasmon resonator," *Phys. Rev. Lett.*, vol. 108, no. 22, p. 226803, 2012.

[25] V. Giannini, A. I. Fernández-Domínguez, Y. Sonnefraud, T. Roschuk, R. Fernández-García, and S. A. Maier, "Controlling light localization and light–matter interactions with nanoplasmonics," *Small*, vol. 6, no. 22, pp. 2498–2507, 2010.

[26] Y. Akahane, T. Asano, B.-S. Song, and S. Noda, "High-Q photonic nanocavity in a two-dimensional photonic crystal," *Nature*, vol. 425, no. 6961, pp. 944–947, 2003.

[27] K. Kishino, M. S. Unlu, J. Chyi, J. Reed, L. Arsenault, and H. Morkoc, "Resonant cavity-enhanced (RCE) photodetectors," *IEEE J. Quant. Electron.*, vol. 27, no. 8, pp. 2025–2034, 1991.

[28] Y. Liu, R. Cheng, L. Liao, et al., "Plasmon resonance enhanced multicolour photodetection by graphene," *Nat. Commun.*, vol. 2, no. 1, pp. 1–7, 2011.

[29] S. Schartner, S. Golka, C. Pflügl, et al., "Band structure mapping of photonic crystal intersubband detectors," *Appl. Phys. Lett.*, vol. 89, no. 15, p. 151107, 2006.

[30] K. Posani, V. Tripathi, S. Annamalai, et al., "Nanoscale quantum dot infrared sensors with photonic crystal cavity," *Appl. Phys. Lett.*, vol. 88, no. 15, p. 151104, 2006.

[31] S. Kalchmair, H. Detz, G. Cole, et al., "Photonic crystal slab quantum well infrared photodetector," *Appl. Phys. Lett.*, vol. 98, no. 1, p. 011105, 2011.

[32] R. Gansch, S. Kalchmair, P. Genevet, et al., "Measurement of bound states in the continuum by a detector embedded in a photonic crystal," *Light Sci. Appl.*, vol. 5, no. 9, pp. e16147–e16147, 2016.

[33] A. Kodigala, T. Lepetit, Q. Gu, B. Bahari, Y. Fainman, and B. Kanté, "Lasing action from photonic bound states in continuum," *Nature*, vol. 541, no. 7636, pp. 196–199, 2017.

[34] Z. Liu and R. Magnusson, "Concept of multiorder multimode resonant optical filters," *IEEE Photonics Technol. Lett.*, vol. 14, no. 8, pp. 1091–1093, 2002.

[35] M. Shokooh-Saremi and R. Magnusson, "Wideband leaky-mode resonance reflectors: influence of grating profile and sublayers," *Opt. Express*, vol. 16, no. 22, pp. 18249–18263, 2008.

[36] S. Fan and J. D. Joannopoulos, "Analysis of guided resonances in photonic crystal slabs," *Phys. Rev. B*, vol. 65, no. 23, p. 235112, 2002.

[37] J. Jin, X. Yin, L. Ni, M. Soljačić, B. Zhen, and C. Peng, "Topologically enabled ultrahigh-Q guided resonances robust to out-of-plane scattering," *Nature*, vol. 574, no. 7779, pp. 501–504, 2019.

[38] F. Ren, K.-Y. Kim, X. Chong, and A. X. Wang, "Effect of finite metallic grating size on Rayleigh anomaly-surface plasmon polariton resonances," *Opt. Express*, vol. 23, no. 22, pp. 28868–28873, 2015.

[39] Y. Yang, I. I. Kravchenko, D. P. Briggs, and J. Valentine, "All-dielectric metasurface analogue of electromagnetically induced transparency," *Nat. Commun.*, vol. 5, no. 1, p. 5753, 2014.

[40] M. G. Saber, G. Vall-Llosera, D. Patel, et al., "Silicon-based optical links using novel direct detection, coherent detection and dual polarization methods for new generation transport architectures," *Opt. Commun.*, vol. 450, pp. 48–60, 2019.